Effect of welding parameters on morphology and mechanical properties of Ti–6Al–4V laser beam welded butt joints

A. Squillace, U. Prisco*, S. Ciliberto, A. Astarita

Department of Materials and Production Engineering, University of Napoli Federico II, Piazzale Tecchio, 80, 80125 Napoli, Italy

ARTICLE INFO

ABSTRACT

The influence of welding speed and laser power on weld quality of 1.6 mm thick $Ti-6Al-4V$ sheets autogenously laser beam welded in butt configuration using a Nd-YAG laser was studied. The joint quality was characterized in terms of weld morphology, microstructure and mechanical properties. An underfill defect, controlling the whole weld geometry, was observed both at the weld face and root surface. In dependence of the specific heat input, this defect showed a maximum, which separates two different welding regimes: keyhole welding, at low heat input, and a welding regime where heat conduction around the keyhole is predominant, at high heat input. Influence of the underfill radius on the weld fatigue life was also assessed.

© 2011 Elsevier B.V. All rights reserved.

1. Introduction

Due to their high strength-to-weight ratio, corrosion resistance, creep performance and compatibility with carbon fibre composite, titanium alloys have been recently used in substitution of aluminium alloys in the aerospace industries. Titanium alloys can also replace aluminium alloys when the operating temperature is higher than 130 °C or when the use of different material lead to an excessive volume of the final part, e.g. for the landing gear of the Boeing commercial aircraft 747 and 757 (Boyer, 1996). Among commercial titanium alloys, the $\alpha + \beta$ grade 5 Ti–6Al–4V alloy is the mainly employed thanks to its favourable combination of physical and mechanical properties, also considering that Ti–6Al–4V can be strengthened by heat treatment or by thermomechanical processing.

However, titanium alloys are more expensive than aluminium ones owing both to the higher price of the raw material and to the complexity of the forming and machining process that they necessitate. Under these respects, welding becomes an interesting technology aiming at cost reduction and enhancement of production output (Donachie, 1989); obviously, so that welding could replace traditional manufacturing technology, such as forming and machining, it is required that the quality of the produced joints be guaranteed.

So far, many energy sources have been considered for titanium welding (Short, 2009). For its capability of delivering high energy on small surface, laser beam welding (LBW) is a satisfactory candidate as power source for high quality titanium welding in different set up, as shown by Li et al. (1997). As reported by Mendez and Eagar (2002), the trend in the aerospace industries is to use diffusely the welding in place of the riveting to reach weight and cost reduction; this new scenario, related with the increasing incidence of polymer matrix composite, turn the welding of titanium alloys into an essential topic of the aerospace research.

Wang et al. (2003) showed that laser beam welded Ti–6Al–4V sheet reach good mechanical properties even if tests temperature rises up to 450 °C. Cao and Jahazi (2009) proved that Nd:YAG laser is an applicable source of laser power for welding titanium, even if morphology of the weld bead strongly depends on welding speed. Kabir et al. (2010) focused their attention on the defocusing distance and welding speed consequences on transverse weld geometry; they found that both parameters could be optimized in order to achieve good quality joint with low geometry defects.

In the present paper, the effects of laser parameters, in particular welding speed and laser power, on the final quality of butt joints in Ti–6Al–4V alloy is experimentally determined. The three main task of the study are to:

- determine the influence of welding parameters on weld morphology and try to explain the origin of the main geometrical features, as underfill, face and root reinforcements;
- evaluate the influence of welding parameters on heat affected zone (HAZ) and fusion zone (FZ) extent, microstructural characteristics and local hardness profiles;

* Corresponding author. Tel.: +39 0817682336; fax: +39 0817682362; mobile: +39 3346990432.
 E-mail address: umberto.prisco@unina.it (U. Prisco).

Table 1
Chemical compositions of the Ti–6Al–4V (weight percent, wt%).

	Al	V	Fe	O	N	C	H	Others
Ti–6Al–4V	5.50–6.75	3.5–4.5	<0.4	<0.2	<0.03	<0.005	<0.003	<0.10
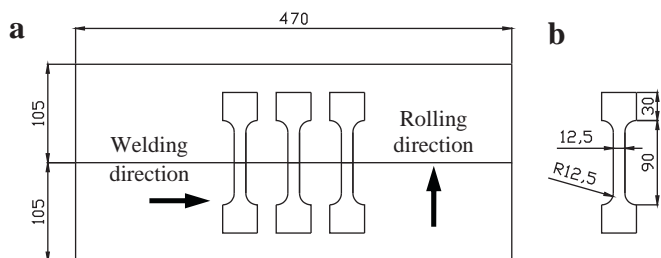
Fig. 1. (a) Scheme of welding with respect to the rolling direction and extraction of tensile specimens and (b) dimensions of tensile specimen according ASTM E8M-04 (all dimensions are in 'mm').

Table 2
Mechanical properties of the Ti–6Al–4V along the rolling direction. The 95% confidence limits (±2 std. dev.) are reported.

Modulus of elasticity	113 ± 2 GPa
Yield strength	891 ± 39 MPa
Ultimate tensile strength	964 ± 42 MPa
Elongation at break	14 ± 0.8%
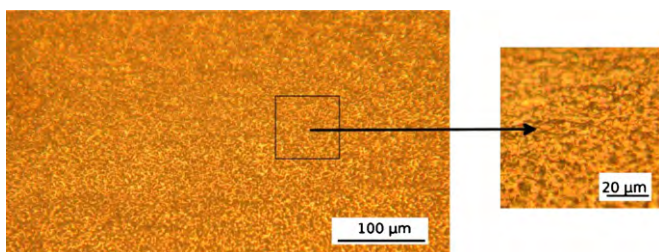
Fig. 2. microstructure of the Ti–6Al–4V base material: inter-granular β phase (black) in an equiaxed α phase (white); L-ST orientation with respect to the rolling direction.

- assess the influence of the welding parameters and weld morphology on mechanical properties of the joints, in particular tensile and fatigue strength.

2. Experimental procedures

Mill-annealed sheets (470 mm × 105 mm) of 1.6 mm thick Ti–6Al–4V (ASTM B265 Grade5) were autogenously laser beam welded using a 2 kW continuous wave solid state Nd-YAG laser. To this purpose, a ROFIN SINCAR CW 020 system equipped with a MOTOMAN UP-20 robotized arm was employed. The weld was performed perpendicular to the rolling direction, see Fig. 1. The chemical composition and mechanical properties of the base alloy are given in Tables 1 and 2. Fig. 2 reports a micrograph of the base material (BM) observed in a section perpendicular to the welding direction, i.e. longitudinal-short transverse (L-ST) orientation with respect to the rolling direction. The microstructure of the base material looks fairly well recrystallized containing only a few stringers with a deformed lamellar, unrecrystallized appearance; the microstructure is composed of a β phase dispersed in a dominating α matrix; in particular, the β phase is distributed at the boundaries of basically equiaxed α grains. This is a classical mill-annealed microstructure for an $\alpha-\beta$ titanium alloy (Lutjering and Williams, 2003).

A collimation lens, a focal lens and an optical fibre of 120, 80 and 0.6 mm in diameter, respectively, were used to produce a focal spot of approximately 0.4 mm. To avoid reaction between the molten metal and the atmospheric oxygen, the weld bead was carefully shielded with protection gas on both side of the laminate; specifically, the top of the weld was protected by 200 Nl/h of high pure helium while argon at flow rate of 200 Nl/h was used for the weld root. In order to fend off every contamination by external undesired solid, the surfaces of the sheet were brushed and cleaned whit methanol prior to the clamping in weldment setup. To obtain a full penetration of the thickness, the laser beam was focused 0.25 mm over the surface of the sheet.

To investigate the effect of the welding parameters on the macroscopic geometry, microstructure and mechanical properties of the butt joints, the welds were manufactured at various values of welding speed and laser power. The welding speeds ranged between 17 and 58 mm/s with steps of around 8 m/s; specifically, the following values of the welding speed were adopted: 17, 25, 34, 42, 50 and 58 mm/s. Three level of the laser power were investigated: 0.8, 1 and 1.2 kW. Unfortunately, not all the combinations of welding speed and laser power resulted workable, i.e. led to successful welds. Indeed, at low welding speeds, using high values of laser powers (e.g., at 17 mm/s with laser power of 1 or 1.2 kW) resulted in an excessive melting with subsequent weld pool instability and weld dropout. On the other side, when the welding speed was high and the laser power too low (e.g., at 58 mm/s with laser power of 0.8 or 1 kW), lack of penetration occurred due to an insufficient power density. Successful combinations of welding speed and laser power are reported in Table 3. Hence, a total of 10 welds were performed.

From each weld, three metallurgical specimens with the main surface perpendicular to the welding direction were cut away from the welded sheets to record macroscopic weld geometry, microstructure and to perform the microhardness test. Every metallurgical specimen was mounted in a proper thermoset resin and, then, polished with grinding discs until surface exhibited a mirror-like finish. Afterward, the samples were etched by Kroll's reagent (2 ml HF, 6 ml HNO$_3$ and H$_2$O up to 100 ml) to unveil the significant features of the metallurgical microstructures, in particular grain boundaries and phase distribution. The optical observations were

Table 3
Combinations of welding speed and laser power resulting in successful welds; SW, successful weld.

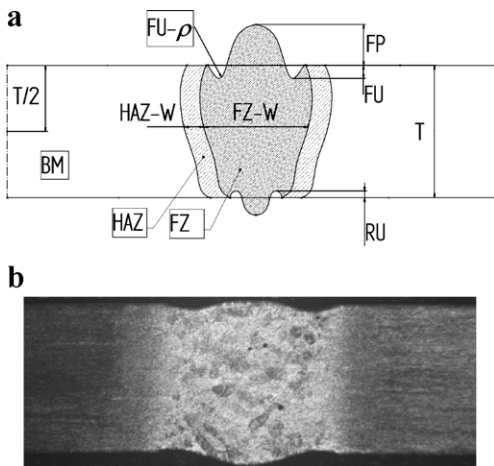| Laser power [kW]	Welding speed [mm/s]					
	17	25	34	42	50	58
0.8	SW	SW	SW	Lack of penetration	Lack of penetration	Lack of penetration
1.0	Dropout	SW	SW	SW	SW	Lack of penetration
1.2	Dropout	Dropout	Dropout	SW	SW	SW

Fig. 3. (a) Sketch of the typical cross section of the obtained welds showing the measurements performed on each sample. FU: face underfill, RU: root underfill, FU-ρ: face underfill radius, FZ-W: fusion zone width, HAZ-W: heat affected zone width; (b) macrograph of a typical cross section (weld at 1.2 kW, 42 mm/s).

carried out using an inverted metallurgical microscope (Olympus GX71) equipped with an Olympus digital camera (XC50); Vikers microindentation hardness was measured using a load of 500 g and spacing between indentations of 0.2 mm. Geometrical measures (size, area, radius, shapes, etc.) of the FZ, HAZ and observed defects were performed through image analysis of the transverse section morphology of each weld.

To gain information about tensile properties of the weldments, four tensile specimens with the axis oriented perpendicular to the welding direction, i.e. parallel to the rolling direction, see Fig. 1, were cut away according to ASTM E8M-04; tensile tests were performed at a strain rate of 10^{-4} s^{-1} on a MTS servo-hydraulic testing machine.

To study the importance of the underfill radius onto the fatigue life of the joints, two sets of twelve specimens, obtained using different welding parameters, were employed for constant load amplitude fatigue tests according to ASTM E466-82. In particular, the two twelve-joint sets were welded with welding speed and laser power of 17 mm/s, 0.8 kW and 25 mm/s, 1.2 kW, respectively. Fatigue specimens have main axis perpendicular to the welding direction. Three levels of maximum stress were selected for the fatigue tests: 80%, 60% and 40% of each weld's respective UTS. The specimens were cycled sinusoidally at 10 Hz frequency and at the stress ratio $R = 0.1$. For each maximum stress level, four welds were tested. Fatigue tests were performed on the same universal MTS-testing system.

3. Result and discussion

3.1. Morphology of the welds

All the obtained welds present the same morphological aspect, which is sketched in Fig. 3. In particular, the centre of the FZ, both at the weld face and root surface, humps into a convex shape that results into a peak manifestly protruding from the baseplate surface of the sheets. The peaked centre of the FZ is in agreement with which was observed by Cao and Jahazi (2009) and also by Kabir et al. (2010). The presence of this welding defect could not be eliminated even though different welding parameters were adopted.

Underfill defects, symmetrically located at the right and left side of the FZ, are also observed on both the top and bottom of the weld transverse sections, see Fig. 3. As for the peaked FZ, the control of the laser power density by changing the welding parameters object of this study did not result in welds completely free of underfill.

Some authors improperly call undercut this kind of defect, classifying it as a curved undercut, opposed to the crack-like and the micro-flaw undercut, see (Nguyen and Wahab, 1998) and (Pastor et al., 1999). Actually, the observed defect is "a groove weld condition in which the weld face or root surface is below the adjacent surface of the base metal" (AWS A3.0:2001., 2001). This condition is defined underfill by the America Welding Society (AWS). On the other side, according to the AWS, the undercut is "a groove melted into the base metal adjacent to the weld toe or weld root and left unfilled by weld metal".

The observed complex shape of the weld beads is due to the synergy of different physical phenomena: volume contraction, surface tension, gravity, vapour pressure and phase transformation. Because of the complexity of the physical phenomena involved, a quantitative satisfactory understanding of the evolution of the wavy shape at the top and bottom of the weld pool does not exist at the present time (Pastor et al., 1999). However, the forces playing the main role in the distribution of the molten metal and, then, in the formation of the underfill and of the humped bead are:

(a) evaporation and expulsion of the molten materials due to the action of the high power density;
(b) contact angle between the solid base alloy and the weld pool at the three-phase contact line of the weld toe and root;
(c) phase transformation, which implies variation of the specific volume of the involved phases.

The evaporation of materials is always present during LBW, while material expulsion can occur when the vapour pressure in the keyhole increases above a certain level, at which the flow of gas can carry some liquid metal outside or can open a conduit at the bottom of the weld, as discussed by (Pastor et al., 1999) and (Dawes, 1992). As the laser beam moves forward, underfill can form if the molten metal cannot refill all the depressions formed by materials expulsion. This is the so-called spattering phenomenon. With regard to this phenomenon, it is obvious that increasing the specific heat input the welding spatter increases and results in an increase of the underfill. However, during this work, no evidence of spattering was observed.

The contact angle at the pool edges depends on surface tension of the interfaces among adjacent phases. It is difficult to predict the value of this angle because of the surface-tension gradients induced by the temperature gradients along the pool surface; indeed, the temperature of the pool surface is significantly higher at the centre than at the edge. However, it is known that the contact angle is determined not only by the surface tension effect in the molten material, but also predominantly by the laser beam size and spatial power density distribution (Aalderink et al., 2007). Furthermore, surface-tension gradients induce the Marangoni convection in the weld pool, which drives the liquid at the pool surface from regions of low surface tension to region of high surface tension, i.e. from the centre to the boundary of the weld pool (Aalderink et al., 2007) and (Fabbro, 2010). Then, by modifying the surface tension, the contact angle varies as well, the global behaviour of the molten alloy being drastically changed.

Phase transition of the Ti–6Al–4V alloy from solid (density at room temperature ≈ 4.42 g/cm^3) to liquid (density at melting point ≈ 3.8 g/cm^3) causes an increase of specific volume of around 16%. The variation can be estimated to reach around 20% if superheating of the molten alloy is considered. This means that the liquid mass cannot settle within its original volume but gets over the surface of the base material at weld top and bottom. Naturally, solidification and cooling of the FZ implies a contraction having the opposite effect on the material of the weld pool.

The underfill defect not only influences the appearance of weld beads, but also causes a stress concentration at the weld edges,
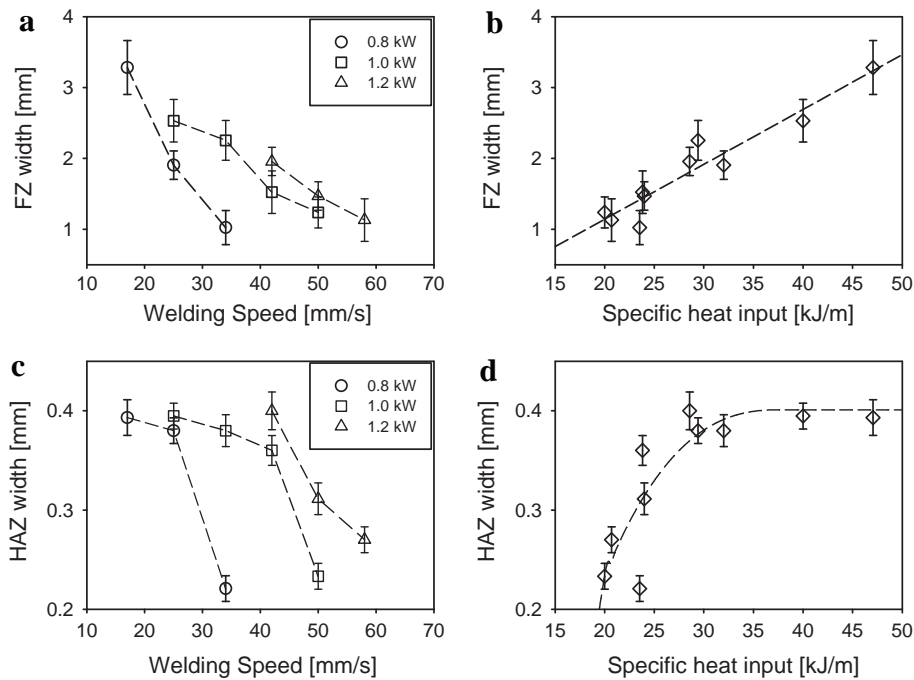
Fig. 4. Average FZ width as function of (a) welding speed at different laser powers and (b) specific heat input; HAZ width as function of (c) welding speed at different laser powers and (d) specific heat input. Error bars indicate 80% confidence limits.

which has a great effect on the reliability of the weld joints. Indeed, the maximum depth of the underfill is strictly limited by several international authorities; for example, as suggest by AWS D17.1 (AWS, 2001), the maximum allowed underfill depth for welded aerospace joint is 7% of the total thickens of the sheet for a Class A welds. For the thickness used in this study, a maximum underfill depth of 0.112 mm could be accepted for a Class A joint; according to this limit, all produced welds meet the needing of class A, see below. To study the stress concentration effect on the weld mechanical performances due to the underfill, besides underfill depths, the underfill radius at the top and bottom of the weld bead was measured. This radius is found drawing the osculating circle of the weld profile at the underfill bottom, see Fig. 3; this radius is known to be the main reason of the toe and root region susceptibility to fatigue loading, as reported by (Nguyen and Wahab, 1998) and (Fricke, 2003).

However, the abovementioned defects apart, transverse sections of all joints show a fully penetrated sound weld with no macroscopic porosity. Moreover, in spite of the high heat input used in this study, no presence of drop out was recorded.

For each welding condition, at least three weld cross-sections were analyzed to obtain weld dimensions including (see Fig. 3):

- face underfill: underfill depth measured at the weld face;
- root underfill: underfill depth measured at the root surface;
- face underfill radius: radius of the underfill at the weld face;
- root underfill radius: radius of the underfill at the root surface;
- FZ width: width of the FZ measured at the middle of the weld;
- HAZ width: width of the HAZ measured at the middle of the weld.

The geometrical characteristics of the welds reported in the followings represent then values averaged over three measurements. But, in the case of the weld geometrical characteristics symmetrically situated at the right and left side of the weld, as face underfill, root underfill, face underfill radius, root underfill radius, both values were measured for each sample and, then, values reported in the followings are means over six measurements.

The extent of the FZ and of the HAZ measured at the middle of the weld, as functions of the welding speed are shown in Fig. 4(a) and (c) for different nominal laser power. The influence of specific heat input on FZ and HAZ is given Fig. 4(b) and (d); dashed best fit-curves are reported to show the overall trend of the FZ and HAZ widths with the specific heat input. It is observed that the FZ width is relatively wide at low welding speed for all laser power, the larger value (∼3.3 mm) being registered at 0.8 kW and 17 mm/s, and narrows with increasing welding speed to about the same value, ∼1 mm, reached at the maximum welding speed for each laser power. However, the more pronounced drop of the FZ width with the welding speed is observed at laser power of 0.8 kW while at 1 and 1.2 kW the curves of Fig. 4 look more or less parallel. Moreover, the width of the FZ exhibits a clear linear trend with the heat input. This behaviour is expected considering that doubling the specific heat input results in the melting of a double quantity of metal.

The HAZ width clearly decreases increasing the welding speed at all laser power, see Fig. 4(c). However, the trends of the HAZ width versus specific heat input, reported in Fig. 4(d), show a kind of saturation effect. Indeed, the HAZ width reaches a maximum of around 0.4 mm when specific heat input attains 30 kJ/m; this behaviour is also reported by (Cao and Jahazi, 2009) and could be related to the formation of a conduction FZ surrounding the keyhole FZ; when the heat input increases, the conduction FZ growths while the HAZ remains at his maximum value.

Fig. 5(a) and (c) report the underfill depth as function of the welding speed for different laser powers. The underfill depth was measured both at the weld face and root surface, face underfill and root underfill, respectively. Fig. 5 evidently shows that both the face underfill and root underfill first increase and, reached a maximum value, decrease with the welding speed. In particular, the maximum underfill depth shifts towards larger welding speed increasing the laser power. In fact, the complete trend of the underfill versus welding speed is visible only at the intermediate value of the laser power, i.e. at 1 kW, where face underfill and root underfill show a maximum of about 0.06 mm for welding speeds equal to 42 and 33 mm/s,
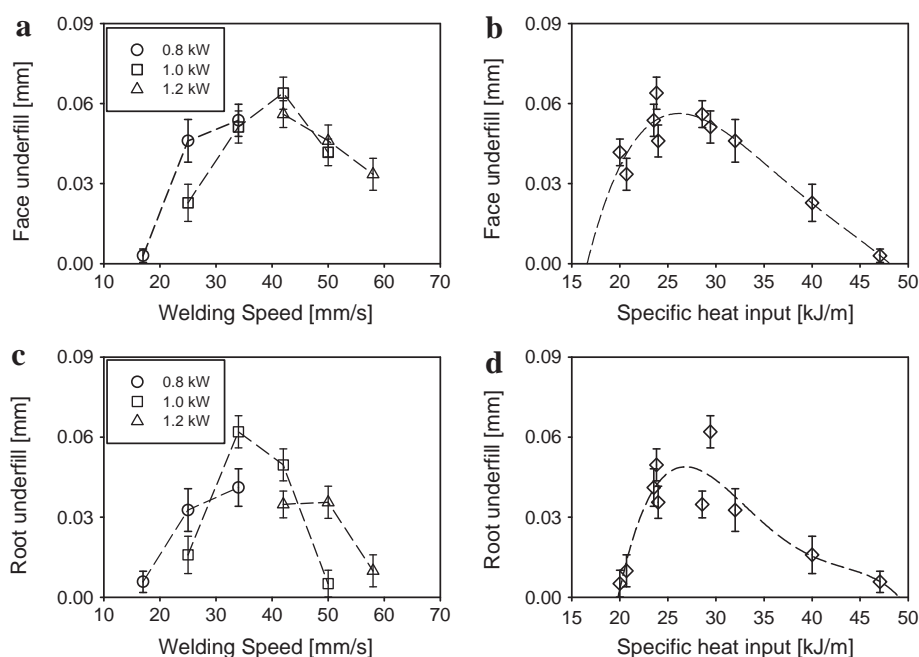
Fig. 5. Average face underfill as function of (a) welding speed at different laser powers and (b) specific heat input; average root underfill as function of (c) welding speed at different laser powers and (d) specific heat input. Error bars indicate 80% confidence limits.

respectively. At laser power of 0.8 and 1.2 kW, the descending and rising branches, respectively, of the curves are not fully visible being located on range of welding speed and laser power combinations which resulted in unsuccessful welds, as discussed above. The previously mentioned behaviour of the underfill defect is completely confirmed by Fig. 5(b) and (d) reporting the underfill depth as function of the specific heat input. This behaviour not yet completely understood was already observed for different materials and now it is confirmed, for the first time to author's knowledge, for Ti–6Al–4V. Synthesizing different explanations so far proposed, and in particular referring to Aalderink et al. (2007) and Fabbro (2010), the following explanation of the underfill trend in dependence of the welding speed and laser power is now proposed. The indubitable phenomena are the followings:

(1) the keyhole elongation decreases with the welding speed, namely decreasing the specific heat input (Aalderink et al., 2007) and (Fabbro, 2010);
(2) at regime of high welding speed, i.e. low values of the specific heat input, two side flows originating from the keyhole front wall start to become very important and to collide with the central emerging flow (Fabbro, 2010).

Both the keyhole elongation and the two side flows bring about the underfill defect, but in different ways. The elongation of the keyhole increases the path the molten has to travel up to the keyhole end and, then, extends its time of cooling down before the two main molten flows come together at the keyhole end. On the other way, the two side flows, colliding with the central emerging flow, prevent it from reach the sample surface near the interface between the keyhole and the solid material.

At low welding speed regimes, then, the increase of the underfill depth with the welding speed is due to the superposition of the abovementioned phenomena. Beyond the welding speed resulting in the largest underfill, the decrement of the keyhole elongation overcomes the increment of the side flow and, then, an underfill decrease is registered, see Fig. 5. The shift to right of the underfill maximum confirms the previous hypothesis; indeed, increasing the

laser power, the two side flows and their influence on the underfill increases.

The underfill radius being the main reason of stress concentration effects deserves special attentions. It is well known that problems can resulted when there is an abrupt change in section caused by excessive weld reinforcement, inclusion of slag or lack of penetration but especially by the underfill (Fricke, 2003). In particular, the underfill radius, along with adverse metallurgical conditions such as tensile residual stresses and coarse HAZ microstructures, is the main reason for root and toe cracking, especially under fatigue loading, see (Balasubramaniana et al., 2000) and (Nguyen and Wahab, 1998). Fig. 6 reports the underfill radius measured at the weld face and root surface, respectively, as function of the welding speed and specific heat input. The underfill radius clearly decreases with the welding speed both at the weld face and root surface, i.e. it increases while the specific heat input rises. This behaviour is related to the widening of the FZ brought about by the higher specific heat input and, consequently, to the larger quantity of molten metal and to its higher temperature, i.e. lower viscosity and surface tension. Hence, the specific volume decrease under phase transition from liquid to solid metal at the FZ-HAZ interface can be counterbalanced by the good deal of overheated molten metal acting as a feedhead which, in this condition, is also capable of filling up the underfill, previously created. It is interesting to notice that both the face and root underfill radii reach a plateau at low value of the specific heat input. This is due to limited extension of the FZ and to the little underfill depth which are registered at this low specific heat input.

Experimental results about weld morphology clearly suggest that two different welding regimes are encountered increasing the specific heat input. For specific heat input lower than 25 kJ/m, the typical keyhole welding is observed. Experimental evidences that confirm the previous hypothesis are the low values of the FZ, HAZ, underfill and underfill radius which are distinctive of this kind of regime. In particular, in keyhole regime, the HAZ and the underfill increase with the specific heat input. For specific heat input higher than 25 kJ/m, heat transport phenomena founded more on conduction around the keyhole than on the classical convective
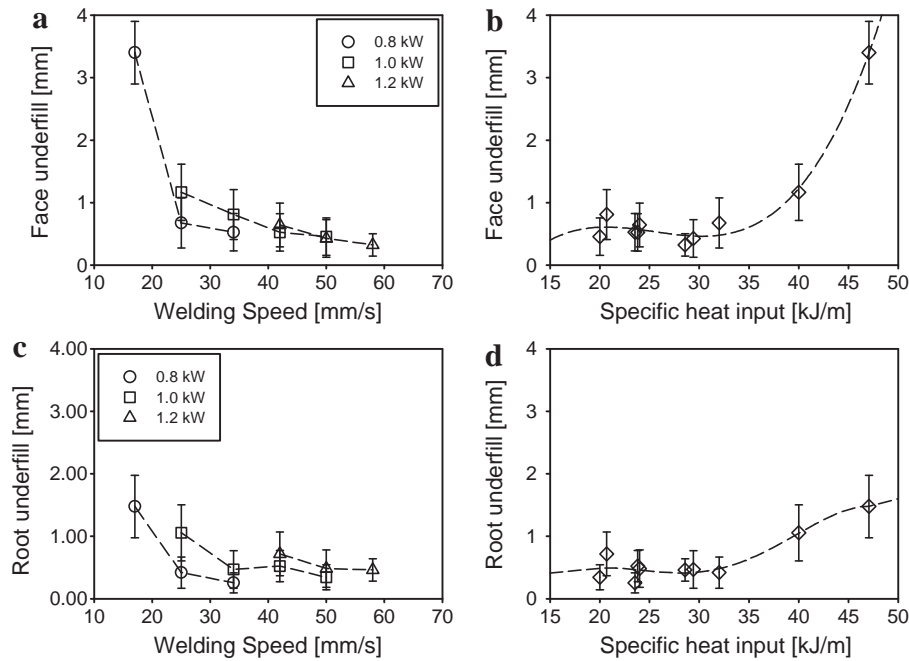
Fig. 6. Average face underfill radius as function of (a) welding speed at different laser powers and (b) specific heat input; average root underfill radius as function of (c) welding speed at different laser powers and (d) specific heat input. Error bars indicate 80% confidence limits.

mechanisms within the keyhole rise of importance. According to the experimental observations, this brings on an increment of the FZ and a decrement of the underfill while the underfill radius tends to increase. Between 25 and 30 kJ/m, a mixed regime, where the abovementioned mechanisms have the same importance, is attained, as testified by the maximum reached by both the face and root underfill. Above 30 kJ/m, the welding is strictly ruled by the heat conduction around the keyhole whereby most part of the FZ is generated by just this mechanism of heat transport. This makes the HAZ width to reach the saturation level, as above reported. In this conduction-predominant regime, the underfill decreases and, as a consequence, the underfill radius grows with the specific heat input.

3.2. Microstructures

During laser beam welding the joint region undergoes a great thermal gradient from the weld pool to the base material; this spatial and temporal distribution of temperature produces a non uniform microstructure. As shown in Fig. 7, three different zones are visible for each weld: base material, HAZ and FZ.
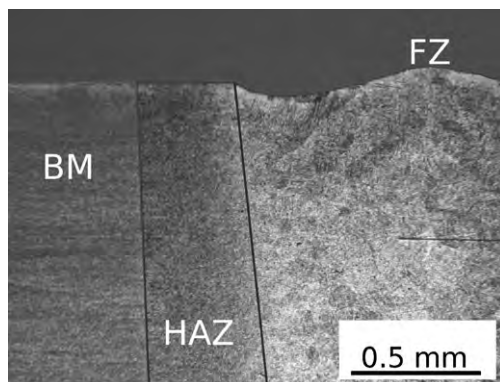

Fig. 7. Macrograph of the weld transverse section at 0.8 kW and 17 mm/s.

The microstructure evolution of the FZ during cooling, magnified in Fig. 8, is the following: during the solidification phase, bcc β dendritic grains growth in the direction of the heat flow (Wang et al., 2003); when the temperature reach the β transus (i.e. 980 °C), diffusionless transformation from β to α' martensitic structure occurs when the cooling rate is high enough (Ahmed and Rack, 1998). As shown by Fig. 8, no α structure is developed from the prior β grains for the maximum and minimum specific heat input condition which result in the higher, Fig. 8 (a), and lower, Fig. 8 (b), cooling rate, respectively (Short, 2009). In these cases, the cooling rate is always above the critical cooling rate of 410 °C/s (Ahmed and Rack, 1998) which allows the formation of a full martensitic α' structure. The microstructure evolution observed is a straightforward result of the thin thickness of the sheet that causes a rapid cooling rate even for the lower specific heat input condition.

The HAZ microstructure is more complex and contains some features not present in the FZ, see Fig. 9. The HAZ seems to be characteristic of a Ti–6Al–4V alloy quenched from a temperature below the β transus, where the complete transformation $\alpha \rightarrow \beta$ is attained; nevertheless, the observed difference between the BM and HAZ microstructures suggests that the HAZ always crossed 450 °C, where the α/β phase equilibrium is attained. From 450 °C to β transus (~980 °C), the equilibrium fraction of β increases and, eventually, reaches unity (Elmer et al., 2004).

When some α transforms in β, the subsequent evolution of the structure is dictated by the cooling rate (Ahmed and Rack, 1998). The highest cooling rate surely takes place in the HAZ region adjacent to the FZ; indeed, this region presents the microstructure more different from the BM, showing the characteristic long orthogonally oriented martensitic plates of α' having an acicular morphology. The presence of α' within the HAZ of a Ti–6Al–4V weld was already proved by Cao and Jahazi (2009), Wang et al. (2003), Akman et al. (2009) and Zhao et al. (2011). However, depending on the distance from the FZ, the HAZ reaches different temperatures and undergoes different cooling rates. As a consequence, inside the HAZ, the microstructure evolves from a rich α' region near the weld bead to a poor α' region near the BM where the lowest temperature and cooling rate are registered. This gradient of α' content is, then, due
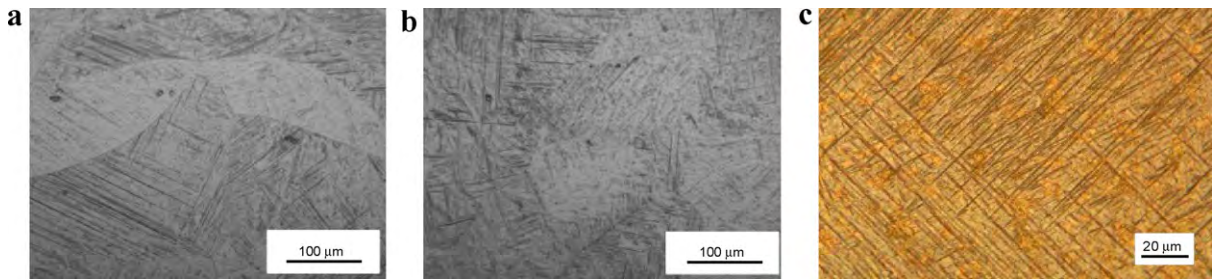
Fig. 8. FZ microstructure of joints welded at (a) 0.8 kW, 17 mm/s and (b) 1 kW, 50 mm/s; (c) is a close-up of the martensitic structure in (b). Martensitic needle-like α' precipitates (dark) are visible within the β grains (light).
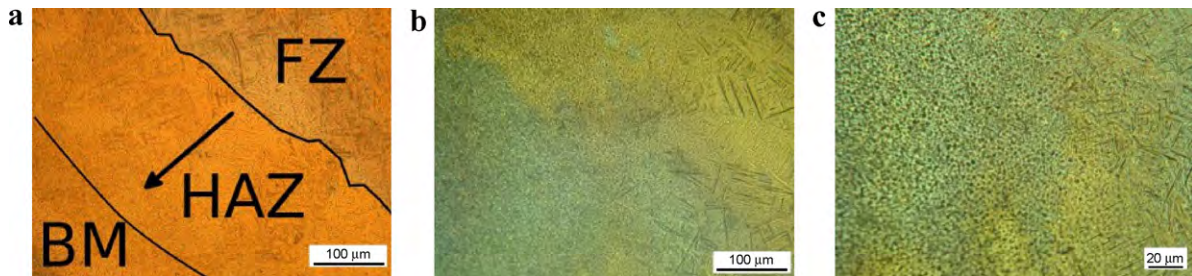
Fig. 9. micrograph of the HAZ at 1 kW and 50 mm/s. (a) Enlarged micrograph of the HAZ; the arrows points from the α'-rich zone adjacent to the FZ to the α'-poor region close to the BM. (b) Microstructure at the interface HAZ/BM (the HAZ is on the right side). (c) Close-up of the microstructure at the interface HAZ/BM (the HAZ is on the right side).

to both temperature and cooling rate gradient that cause a gradation of the solid state transformations occurring inside this narrow zone. Fig. 9 shows the typical HAZ that was obtained in the experimental campaign: a concentration gradient of α' from the FZ to the BM is clearly visible. Similar α' gradient was observed by Cao and Jahazi (2009), Wang et al. (2003), Akman et al. (2009) and Zhao et al. (2011).

However, on the base of the previous discussion, the HAZ is also expected to contain retained β, undissolved primary globular α (which looks like dark points in the micrograph of Fig. 9(b) and (c)) and, where the lowest cooling rates ($\leq 20\,^\circ$C/s) are attained and β exceeds the equilibrium fraction, it is not to rule out the formation of some "basketweave" Widmanstatten α. The content of the different features varies with the distance from the FZ. Naturally, it is very difficult to discriminate the different microstructures of the constituent morphology from a metallurgical analysis based just on optical microscopy over such a small area as the HAZ.

3.3. Microhardness

Fig. 10(b) reports a typical microhardness distribution profile observed on the cross section of the welds. Measurements were performed at the middle, lower and upper part of the cross section, as shown in Fig. 10(a). The microhardness profile reflects the microstructure variations observed in the previous section. The microhardness profile changes from the lowest values in the base material, around 330 ± 10 HV, to the highest value of the FZ. In particular, for each laser power and welding speed combination, the FZ exhibits a microhardness value about 9–17% higher than that of the base material. The higher hardness of the FZ is related to the presence of the martensitic α' structure which exhibits high strength and hardness at expense of ductility and toughness.

As shown in Fig. 11(a), it is found that the mean values of the microhardness in the FZ increase with the welding speed at each laser power level. This trend was also observed by Sun et al. (2002) and is related to the lowering of heat input with the welding speed; this phenomenon causes an increase of the cooling rate (Short, 2009). Indeed, the plot of the microhardness as function of the specific heat input, in Fig. 11(b), clearly reveals that the microhardness decreases increasing the specific heat input.

While the harness is quite uniform in the base material and FZ, inside the HAZ, due to the spatial variation of the microstructure, namely, to the decrease of the martensite content from the FZ boundary to the HAZ/base material interface, the microhardness also decreases. The strong microstructure variation, in addition to the HAZ limited width, leads to a very high spatial gradient of the microhardness. The hardness gradient over the HAZ is reported in Fig. 12 as function of the specific heat input. Points in Fig. 12 are
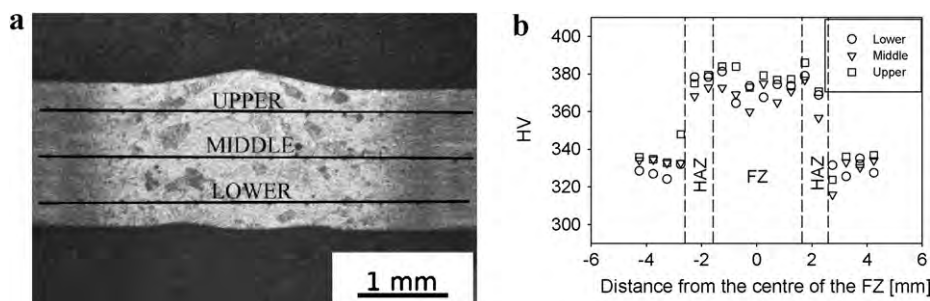

Fig. 10. (a) Location of the microindentations; (b) typical hardness profile observed over the weld cross section (0.8 kW, 17 mm/s, FZ width = 3.3 mm, HAZ width = 0.8 mm).
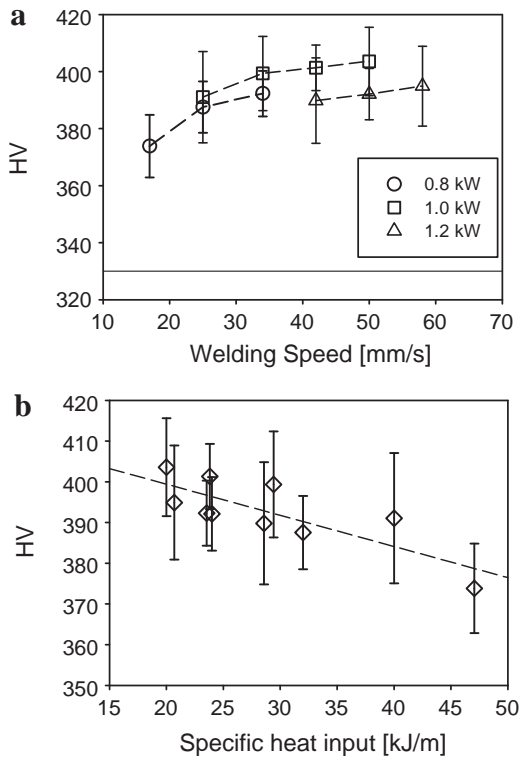
Fig. 11. Mean value of the FZ hardness as function (a) of the welding speed at different laser powers, (b) of the specific heat input. Error bars indicate 80% confidence limits.

calculated, being the hardness gradient the ratio of the hardness difference between the FZ and BM and the HAZ width.

The hardness gradient is inversely proportional to the heat input. Considering that a high hardness gradient is brought about by a high cooling rate, Fig. 12 clearly shows that the higher cooling rates are connected to the lower specific heat inputs. Data are very scattered due to the inhomogeneous microstructure of the HAZ, as above specified. In particular, the gaps in hardness gradients calculated at 20, and 23 kJ/m are brought about by the data spread of the HAZ widths (Fig. 4(d)) and HV of the FZ (Fig. 11(b)) recorded at 20 and 23 kJ/m, even if the HAZ width scatter at 20 and 23 kJ/m played the main role on the indicated gaps. Naturally, the data spread of the HAZ widths decreases as the specific heat input reaches the value of 30 kJ/m where the HAZ attains the abovementioned maximum value. Then, at low specific heat input, the HAZ width data result more scattered.
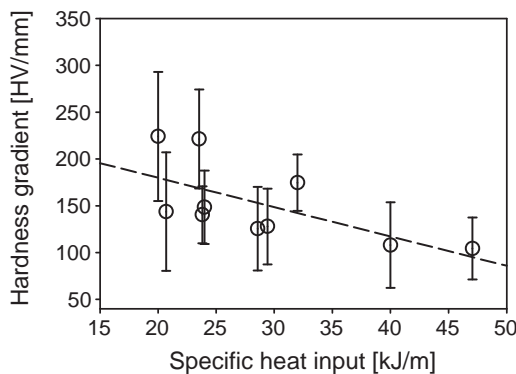
Fig. 12. Average hardness gradient over the HAZ as function of the specific heat input. Error bars indicate 80% confidence limits.

Fig. 13. Tensile specimen welded at 0.8 kW and 17 mm/s.
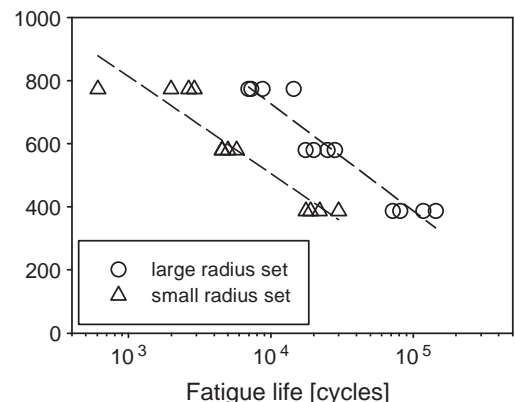
3.4. Tensile test

All tested specimens fractured in the parent metal indicating that geometrical defects did not influence tensile tests and good quality joints were obtained, see Fig. 13 as example. Examination of the fracture surfaces showed that the failure was completely ductile with evidence of necking and orientation of the surfaces at 45° from the tensile axis. Ultimate tensile strength, UTS, 0.2 per cent offset yield strength, YS, and elongation per cent at failure, EL, as function of the welding speed at each power level are summarized in Table 4. UTS and YS data spread around the corresponding mechanical properties of the base material. The presence of the rigid FZ, however, reduces the EL of the welds.

The foregoing tensile data testifies that the welds under investigation, compared with the base material, reach the same tensile performance with a reduced ductility. Ductility loss is quantifiable in a reduction of 21% of the elongation at failure, which drops from 14% to 11%, in average. However, the ductility loss is not dramatic; this makes LBW suitable to gain high performance weld in Ti–6Al–4V.

3.5. Fatigue tests

It is know that the radius of the underfill is a very significant geometrical parameter affecting the fatigue behaviour of a butt joint (Nguyen and Wahab, 1998). Indeed, the fatigue life of butt welded joints can be improved significantly by increasing the underfill radius at weld toes or eliminating the weld toe underfill completely (Fricke, 2003).

The welding parameters to be tested were chosen because the previous discussion about the weld geometry suggested that they supply very different average underfill radii at the weld top and bottom. Indeed, at 17 mm/s and 0.8 kW the average underfill radii are 3.5 mm and 1.5 mm at the weld top and bottom, respectively. On the other hand, at 25 mm/s and 1.2 kW the average underfill radii are 0.1 mm and 0.5 mm at the weld top and bottom, respectively. Hereinafter, the set of specimens welded at 17 mm/s and 0.8 kW will be called large radius set while the set of specimens welded at 25 mm/s and 1.2 kW will be called small radius set. Fig. 14 shows the obtained S–N curve, maximum stress versus cycles to failure, where the effect of the underfill radius is clearly evident. Indeed,

Fig. 14. S–N curves of the two sets of welds tested under fatigue.

Table 4
Results of the tensile tests. The average values and the 95% confidence limits (±2 std. dev.) are reported.

Laser power [kW]	Welding speed [mm/s]	YS [MPa]	Average YS ± 3 std. dev.	UTS [MPa]	Average UTS ± 3 std. dev.	EL [%]	Average EL ± 3 std. dev.
0.8	17	859		966		6.04	
		837	862 ± 81	943	953 ± 35	6.19	6.16 ± 0.33
		891		950		6.26	
	25	903		950		7.05	
		895	906 ± 38	963	961 ± 30	6.37	6.61 ± 1.14
		920		970		6.41	
	34	908		979		7.09	
		906	907 ± 34	965	960 ± 65	7.21	7.06 ± 0.48
		908		936		6.89	
1.0	25	892		965		7.31	
		926	906 ± 52	952	968 ± 51	7.63	7.43 ± 0.53
		901		986		7.34	
	34	911		975		8.12	
		930	911 ± 58	989	976 ± 39	6.51	7.00 ± 2.92
		891		963		6.36	
	42	918		968		7.26	
		899	921 ± 69	952	971 ± 61	6.16	7.13 ± 2.74
		945		993		7.98	
	50	952		966		9.66	
		973	942 ± 98	1009	974 ± 95	11.36	10.03 ± 3.55
		902		947		9.08	
1.2	42	928		989		10.24	
		961	951 ± 58	950	969 ± 58	8.12	9.25 ± 3.20
		963		968		9.39	
	50	878		990		6.79	
		908	913 ± 113	970	973 ± 48	5.94	6.80 ± 2.59
		953		958		7.67	
	58	891		955		3.23	
		923	909 ± 49	1001	977 ± 69	8.17	4.87 ± 8.57
		913		975		3.21	

the S–N curve tends to move from the left to the right side of the plot as the value of the underfill radius increases; this means that the fatigue strength and fatigue life of butt-welded joints can be improved by either partially or totally eliminating the weld underfill. For example, the fatigue strength at 10^4 cycles is increased by about 35% for the large radius set. On average, the number of cycles to failure of the large radius set at a fixed stress level is increased of around one order of magnitude compared to the small radius counterpart.

Fractographic analysis of the fracture surface produced by the fatigue failure confirms the previous observations. The fracture initiation and propagation is completely different from that which was observed for the monotonic tensile test. Indeed, the fracture started near the lower point of the underfill convexity at the interface between the FZ and the HAZ for all the specimens, see Fig. 15. In particular, for each specimen, the initiation point of the main crack was always observed at the underfill with the smaller radius. Stress concentration realized at the underfill is, then, the main reason of

Fig. 15. Fracture surface of the joint welded at 17 mm/s and 0.8 kW (cycles to failure = 6985, % of UTS = 80%). Propagation surfaces of the main (1) and secondary (2) crack are evidenced.

Fig. 16. fracture surfaces of the joint welded at 25 mm/s and 1.2 kW. (a) cycles to failure = 610, % of UTS = 80%, (b) cycles to failure = 29,890, % of UTS = 40%. Asterisks indicate the crack initiation points.

the fatigue initiation which is known to be very sensitive to local stress peaks. The magnitude of the stress concentration varies with the size and sharpness of the underfill synthesized by the underfill radius. In fact, to give the complete plot, it is to point out that different cracks developing on the same fracture surface were observed in most of the examined cases, see Fig. 16; the cracks tend to be oriented normal to the maximum tensile stress. However, even if many, nevertheless, the cracks are always observed to initiate in the underfill and, then, to follow the weak network of the region adjacent to the grain boundary in the HAZ. Crack propagation within the HAZ are testified by the presence of river markings, see Figs. 15 and 16. In the end, the loss of resistant cross-section, due to crack propagation, caused the final failure that again occurred in a section of the HAZ and that was always observed to be ductile. Partial melting and precipitate formation in the HAZ, along with the presence of the martensite, are surely responsible for the crack propagation in the HAZ upon fatigue testing.

4. Conclusions

Influence of welding speed and laser power on the macroscopic geometry, microstructure, monotonic tensile and fatigue properties of LBW butt joints in Ti–6Al–4V is investigated.

Two welding regimes are observed in dependence of the specific heat input: keyhole welding, for heat inputs lower than 25 kJ/m, and a welding regime where heat conduction around the keyhole is predominant, for heat inputs higher than 30 kJ/m. Furthermore, between 25 and 30 kJ/m, a mixed regime is attained.

All the obtained welds present underfill, face and root reinforcements. Weld morphology is strictly influenced by the welding regime wherein they are produced. In particular, in keyhole regime, the HAZ and the underfill increase with the specific heat input while the underfill radius remains more or less constant. On the other hand, in welding regimes where heat conduction around the keyhole is predominant, the underfill decreases and the underfill radius grows with the specific heat input while the HAZ width reaches a maximum of around 0.4 mm. This means that, in the intermediate mixed regime, the underfill comes to a maximum.

The welds under investigation, compared with the base material, reach similar tensile performance with a reduced ductility.

Fatigue life of the investigated welds is strongly influenced by the value of the underfill radius. Indeed, the *S–N* curve tends to move towards region of higher cycles as the value of the underfill radius increases; this means that the fatigue strength of the welded joints can be improved by partially or totally eliminating the underfill. The fatigue fracture initiates and propagates near the lower point of the underfill convexity at the interface between the FZ and the HAZ.

References

Aalderink, B.J., de Lange, D.F., Aarts, R.G.K.M., Meijer, J., 2007. Keyhole shapes during laser welding of thin metal sheets. J. Phys. D: Appl. Phys. 40, 5388–5393.

Ahmed, T., Rack, H.J., 1998. Phase transformations during cooling in $\alpha + \beta$ titanium alloys. Mater. Sci. Eng. A 243, 206–211.

Akman, E., Demir, A., Canel, T., Sinmazçelik, T., 2009. Laser welding of Ti6Al4V titanium alloys. J. Mater. Process. Technol. 209, 3705–3713.

AWS A3.0:2001., 2001. Standard Welding Terms and Definitions. Including Terms for Adhesive Bonding, Brazing, Soldering, Thermal Cutting, and Thermal Spraying, An American National Standard, Approved by American National Standards Institute. American Welding Society, Miami, FL, 41 pp.

AWS, 2001. Specification for Fusion Welding for Aerospace Application. American Welding Society, Miami, FL.

Balasubramaniana, V., Guhab, B., Swamidasa, A.S.J., Seshadri, R., 2000. Influences of shielded metal arc welded cruciform joint dimensions on toe crack failures of pressure vessel grade steels. Eng. Fail. Anal. 7, 169–179.

Boyer, R.R., 1996. An overview on the use of titanium in the aerospace industry. Mater. Sci. Eng. A 213, 103–114.

Cao, X., Jahazi, M., 2009. Effect of welding speed on butt joint quality of Ti–6Al–4V alloy welded using a high-power Nd:YAG laser. Opt. Laser Eng. 47, 1231–1241.

Dawes, C., 1992. Laser Welding. McGraw-Hill, Inc., New York, USA, 73 pp.

Donachie, M., 1989. Titanium: A Technical Guide. ASM International, Metals Park, OH, pp. 66–70.

Elmer, J.W., Palmer, T.A., Babu, S.S., Zhang, W., DebRoy, T., 2004. Phase transformation dynamics during welding of Ti–6Al–4V. J. Appl. Phys. 95, 8327–8337.

Fabbro, R., 2010. Melt pool and keyhole behaviour analysis for deep penetration laser welding. J. Phys. D: Appl. Phys. 43, 445–501.

Fricke, W., 2003. Fatigue analysis of welded joints: state of development. Mar. Struct. 16, 185–200.

Kabir, A.S.H., Cao, X., Medraj, M., Wanjara, P., Cuddy, J., Birur, A., 2010. Effect of welding speed and defocusing distance on the quality of laser welded Ti–6Al–4V. In: Proceedings of the Materials Science and Technology (MS&T) 2010 Conference, Houston, USA, pp. 2787–2797.

Li, Z., Gobbia, S.L., Norrisb, I., Zolotovskyc, S., Richter, K.H., 1997. Laser welding techniques for titanium alloy sheet. J. Mater. Process. Technol. 65, 203–208.

Lutjering, G., Williams, J.C., 2003. Titanium. Springer-Verlag, Heidelberg, Berlin, pp. 177–194.

Mendez, P.F., Eagar, T.W., 2002. New trends in welding in the aeronautic industry. In: Proceedings of 2nd Conference of New Manufacturing Trends, Bilboa, Spain.

Nguyen, T.N., Wahab, M.A., 1998. The effect of weld geometry and residual stresses on the fatigue of welded joints under combined loading. J. Mater. Process. Technol. 77, 201–208.

Pastor, M., Zhao, H., Martukanitz, R.P., Debroy, T., 1999. Porosity, underfill and magnesium loss during continuous wave Nd:YAG laser welding of thin plates of aluminum alloys 5182 and 5754. Weld. J. 78, 207-s–216-s.

Short, A.B., 2009. Gas tungsten arc welding of $\alpha + \beta$ titanium alloys: a review. Mater. Sci. Technol. 25, 309–324.

Sun, Z., Pan, D., Zhang, W.,2002. Correlation between welding parameters and microstructures in TIG, plasma and laser welded Ti–6Al–4V alloy; trends in welding research. In: Proceedings of the 6th International Conference. ASM International, pp. 760–767.

Wang, S.H., Wei, M.D., Tsay, L.W., 2003. Tensile properties of LBW welds in Ti–6Al–4V alloy at evaluated temperatures below 450 °C. Mater. Lett. 57, 1815–1823.

Zhao, S., Yu, G., He, X., Zhang, Y., Ning, W., 2011. Numerical simulation and experimental investigation of laser overlap welding of Ti6Al4V and 42CrMo. J. Mater. Process. Technol. 211, 530–537.